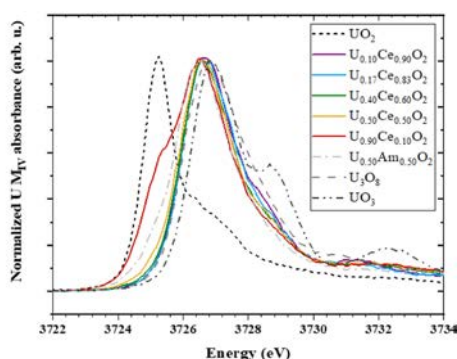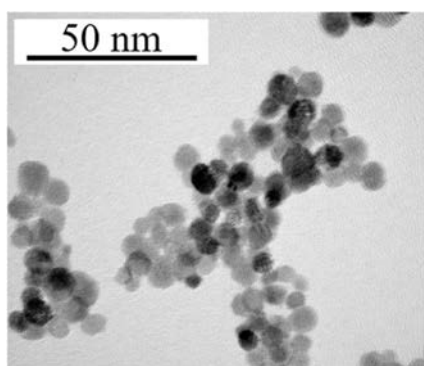# Charge Distribution in U$_{1-x}$Ce$_x$O$_{2+y}$ Nanoparticles

Damien Prieur,* Jean-François Vigier,* Karin Popa, Olaf Walter, Oliver Dieste, Zsolt Varga, Aaron Beck, Tonya Vitova, Andreas C. Scheinost, and Philippe M. Martin

ABSTRACT: In view of safe management of the nuclear wastes, a sound knowledge of the atomic scale properties of U$_{1-x}$M$_x$O$_{2+y}$ nanoparticles is essential. In particular, their cation valences and oxygen stoichiometries are of great interest as these properties drive their diffusion and migration behaviors into the environment. Here, we present an in depth study of U$_{1-x}$Ce$_x$O$_{2+y}$, over the full compositional domain, by combining X ray diffraction and high energy resolution fluorescence detection X ray absorption near edge structure. We show, on one hand, the coexistence of U^{IV}, U^{V}, and U^{VI} and, on the other hand, that the fluorite structure is maintained despite this charge distribution.

INTRODUCTION

Considering that Ce is among the major fission products present in the SNF, which can be incorporated into the UO$_2$ structure, the crystallography of the present chemical phases and the oxidation states of both U and Ce have to be studied as they drive the concomitant release and migration of U$_{1-x}$Ce$_x$O$_{2+y}$ nanoparticles (NPs) in the environment.[1,2]

Due to their structural similarity, uranium and cerium dioxide form a solid solution covering the full compositional range of the Ce content.[3−5] Several articles have been published on the U$_{1-x}$Ce$_x$O$_{2+y}$ properties (electrical con ductivity, magnetic properties, oxygen potential, lattice parameter, heat capacity, thermal expansion, and phase diagram).[3,6−10] Some interesting results have also been reported on both U and Ce valences. Contrary to other substituted UO$_2$ compounds,[11−13] no charge transfer reaction between U^{IV} and Ce^{IV} leading to the formation Ce^{III} and U^{V} has been reported. Indeed, when the mixed oxides are prepared in the right oxygen potential condition to obtain stoichiometric compound U$_{1-x}$Ce$_x$O$_{2.00}$, their lattice parameters closely follow Vegard's law,[8,14] suggesting the progressive substitution of U^{IV} by the Ce^{IV} cation as a function of the composition. Even though there have been several investigations on the redox behavior of Ce doped UO$_2$ mainly on thin films using extreme surface sensitive techniques,[6,7,15] there is none for NP

materials. However, in these latter compounds, the quantum mechanical size effects, combined with a considerable increase of the surface to bulk ratio, may affect the local structure and the charge distribution within the compounds.[16−18] Addition ally, NPs are highly sensitive to room temperature oxidation as they show a considerable surface to bulk ratio.[19]

In this context, the present study aims at studying both U and Ce valences in room temperature oxidized U$_{1-x}$Ce$_x$O$_{2+y}$ NPs. The crystal structure of both as synthesized and room temperature oxidized U$_{1-x}$Ce$_x$O$_{2+y}$ NPs was characterized using X ray diffraction (XRD), giving access to their size and lattice parameter. Furthermore, we probed the electronic structure of the U$_{1-x}$Ce$_x$O$_{2+y}$ NPs using high energy resolution fluorescence detection X ray absorption near edge structure (HERFD−XANES) spectroscopy at both U M$_{IV}$ and Ce L$_{III}$ edges.

EXPERIMENTAL METHODS

Please note that careful attention should be paid for the characterization of these nanocrystalline materials to avoid any energy induced transformations (such as reduction under beam for instance). It has to be mentioned that these materials are radioactive and hence should be manipulated adequately.

Synthesis. The $U_{1-x}Ce_xO_{2+y}$ nanopowders were produced by the decomposition of mixed hydroxides under high temperature water under pressure. $U_{1-x}Ce_x(OH)_4$ ($x = 0-1$) amorphous precipitates were prepared as follows: $2 - 2x$ mL of U^{IV} solution (0.5 M) and $2x$ mL of Ce^{IV} solution (0.5 M) were mixed in test tubes of 50 mL and diluted with 8 mL of distilled water. The coprecipitation was induced with excess (10 mL) of ammonia solution 25% (pH = 14). The precipitates were separated from the alkaline solution and washed repeatedly with distilled water until neutral pH. After washing, the hydroxide precipitates were inserted into Teflon lined hydrothermal synthesis autoclave reactors together with 10 mL of distilled water and reacted for 4 h at 200 °C and 15 bar without stirring. The final product consists (usually) in nanocrystalline $U_{1-x}Ce_xO_{2+y}$ solid solutions which could be easily separated from solution. The nanocrystals were repeatedly washed with ethanol and acetone in order to remove the water potentially absorbed at the surface. Finally, they were dried under the air atmosphere at room temperature for 2 h.

The hydroxide decomposition method under hot compressed water proved to be straightforward in the case of CeO_2, ThO_2, and $U_{1-x}Th_xO_2$ solid solutions.[16,20−22] However, the preparation of $U_{1-x}Ce_xO_{2+y}$ solid solutions through this synthetic route is not always successful, and the method still needs optimization. Thus, we have observed (meta)schoepite like impurities in more than half of the experimental trials, independent of the targeted composition. Potentially different reaction intermediates are formed in this specific case, but the mechanistic study is out of our scope.

The U/Ce ratio (i.e., the stoichiometry) was measured by using a NuPlasma (NU Instruments, Oxford, United Kingdom) double focusing multicollector inductively coupled plasma mass spectrometer. U and Ce monoelemental solutions were used for the calibration of the instrument. For the dissolution, a small amount of the sample was dissolved in 8 M HNO_3 and then successively diluted before the multicollector inductively coupled plasma mass spectrometry (MC ICP−MS) measurement. All dilutions were performed gravimetrically. The results have ±5% relative uncertainty.

The synthetic procedure was performed under an air atmosphere in a fumehood. The products were stored in a desiccator under vacuum after flushing with argon.

X-ray Diffraction. Due to the fast oxidation of the resulting powders, preliminary XRD analyses were performed using a Rigaku MiniFlex 600 diffractometer at the same day of the synthesis. The diffractometer is calibrated with silicon, uses Cu Kα radiation (both $K\alpha_1$ and $K\alpha_2$), and is operated under air. The crystallite size of the nanopowders was estimated from the XRD pattern using the Scherrer equation and averaging the results of eight selected peaks in the 2θ range between 25 and 80°.

The other measurements (done 2 weeks and 3 months after synthesis) used for Rietveld refinement were performed using room temperature XRD analyses performed on about 10 mg of powder with a Bruker D8 ADVANCE diffractometer (Cu Kα radiation, 40 kV, 40 mA) mounted in a Bragg−Brentano configuration. The diffractometer was equipped with a curved Ge(111) Kα1 monochromator, a ceramic copper tube, and a LynxEye position sensitive detector. It is calibrated with the LaB6 reference material (NIST SMR 660b). The diffractometer is installed in a nitrogen atmosphere glovebox, designed to handle highly radiotoxic materials.

With both diffractometers, the XRD patterns were recorded using a step size of 0.02° across the $10° \leq 2\theta \leq 120°$ angular range. Structural analysis was performed by the Rietveld method using Jana2006 software.[23]

Transmission Electron Microscopy. Transmission electron microscopy (TEM) studies were performed using an aberration (image) corrected FEI Titan 80 300 operated at 300 kV. This provides a nominal information limit of 0.8 Å in the TEM mode and a resolution of 1.4 Å in the STEM mode. TEM micrographs have been recorded using a Gatan US1000 slow scan CCD camera. STEM images have been recorded using a Fischione high angle annular dark field detector with a camera length of 195 mm. The samples for analysis have been prepared by dropping coating with a suspension of the NPs in ultrapure water on carbon coated copper grids.

High-Energy Resolution Fluorescence-Detected X-ray Absorption Near-Edge Structure. Inner shell spectroscopy with the use of an X ray emission spectrometer provides an element selective probe of the electronic state and allows observing spectral features with significantly enhanced energy resolution compared to usual data limited by the core hole lifetime broadening.[16,24]

HERFD−XANES measurements were conducted at the CAT ACT beamline (ACT station) of the KIT synchrotron light source (Karlsruhe Institute of Technology, Karlsruhe, Germany).[25,26] The storage ring conditions were 2.5 GeV and 160 mA. Note that these were carried out 3 months after the synthesis. The incident energy was selected using the [111] reflection of a double Si crystal monochromator. The X ray beam was focused to 1×1 mm onto the sample. A slit with a size of 500×500 μm was used in front of the sample in order to further confine the size of the X ray beam on the sample, leading to a slight improvement in the energy resolution. XANES spectra were recorded in the HERFD mode using an X ray emission spectrometer.[24,27] The sample, analyzer crystal, and a single diode VITUS Silicon Drift Detector (KETEK, Germany) were arranged in a vertical Rowland geometry.

The Ce L_{III} HERFD−XANES spectra were obtained by recording the maximum intensity of the Ce $L_{III}-M_V$ emission line (4839 eV) as a function of the incident energy. The emission energy was selected using the ⟨331⟩ reflection of four spherically bent Ge crystal analyzers (with a bending radius $R = 1$ m) aligned at the 80.7° Bragg angle. The molar fractions of Ce^{III} and Ce^{IV} were derived from the linear combination of CeO_2 and Ce^{III} oxalate references.[16]

The U M_{IV} HERFD−XANES spectra were acquired by recording the intensities of U M_4-N_6 (~3337 eV) as a function of the incident energy. The emission energy was selected using the (220) reflection of four spherically bent Si crystal analyzers (with 1 m bending radius) aligned at the 75.4° Bragg angle. The molar fractions of U^{IV}, U^V, and U^{VI} were derived from the linear combination of UO_2, U_4O_9, U_3O_8, β UO_3, and $U_{0.50}Am_{0.50}O_{2-y}$ references 28. 29,

The experimental energy resolutions were 1.15 and 0.85 eV for Ce L_{III} and U M_{IV}, respectively. These were obtained by measuring the full width at half maximum of the elastically scattered incident beam.

The sample, crystals, and detector were set in a box filled with He. A constant He flow was maintained in order to minimize the loss of intensity due to the absorption and scattering of the X rays. The data were not corrected for self absorption effects. The sample exposure to the beam was minimized to account for possible beam damage and checked by first collecting short XANES scans (~10 s) to look for an irradiation effect.

RESULTS AND DISCUSSION

Lattice Parameter and Size of the As-Synthesized NPs. XRD measurements were carried out a few hours after the synthesis.

Our XRD data (cf. Figure 1 of the Supporting Information) show that the as synthesized $U_{1-x}Ce_xO_{2+y}$ crystallizes in the $Fm3m$ fluorite structure (space group 225). Depending on the Ce content, the average crystallite diameters vary from 5 to 13 nm. These XRD refined parameters are gathered in Table 1.

The TEM measurements confirm the XRD data with respect to both phase purity and particle size. As a representative example, Figure 1 shows the morphology of the nanometric $U_{0.50}Ce_{0.5}O_{2+y}$ sample, which is clearly formed by one single family of particles with an average size of 7.3 (1.8) nm. Moreover, energy dispersive X ray (EDX) analysis on

Table 1. Lattice Parameter, Space Group, and Crystallite Size Derived from the Rietveld Refinement[a]

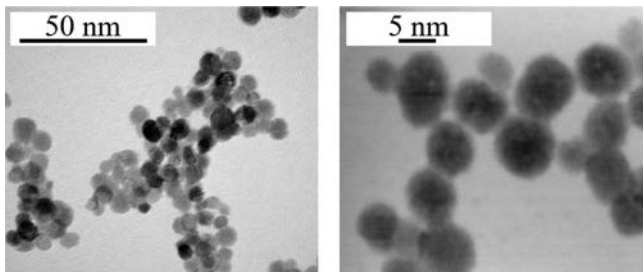|	lattice parameter (Å)	space group	crystallite size (nm)
$U_{0.90}Ce_{0.10}O_{2+y}$	5.460(2)	$Fm\bar{3}m$	13(1.2)
$U_{0.60}Ce_{0.40}O_{2+y}$	5.446(2)	$Fm\bar{3}m$	7.1(0.9)
$U_{0.50}Ce_{0.50}O_{2+y}$	5.441(2)	$Fm\bar{3}m$	7.3(1.0)
$U_{0.40}Ce_{0.60}O_{2+y}$	5.428(2)	$Fm\bar{3}m$	7.1(1.0)
$U_{0.17}Ce_{0.83}O_{2+y}$	5.417(2)	$Fm\bar{3}m$	7.0(0.9)
$U_{0.10}Ce_{0.90}O_{2+y}$	5.413(2)	$Fm\bar{3}m$	5.1(0.6)

[a]Uncertainties are given in brackets.

Figure 1. TEM images of the as synthesized $U_{0.50}Ce_{0.50}O_{2+y}$.

independent particles has confirmed the homogeneity of all the samples as well as their U/Ce ratio.

As can be expected from the literature data,[7,30−33] Figure 2 shows that the lattice parameters of the as synthesized
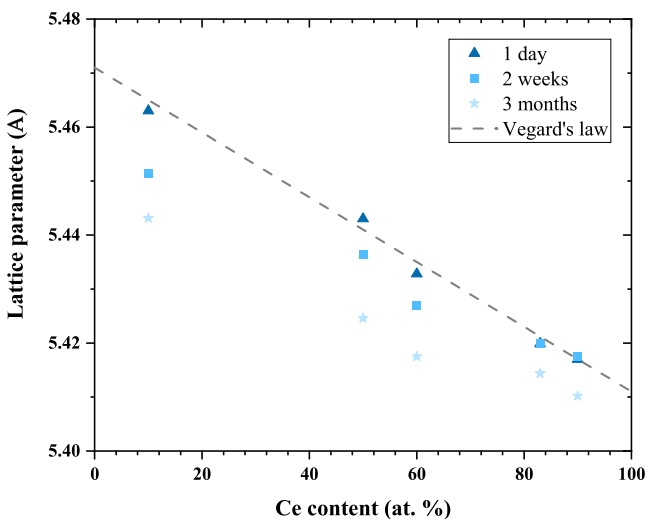

Figure 2. Lattice parameters as a function of Ce content. The lattice parameters of the as synthesized compounds follow Vegard's law (drawn from pure $UO_{2.00}$ and $CeO_{2.00}$ values), while an evolution in time is observed for those collected 1 day, 2 weeks, and 3 months after the synthesis.

compounds follow the UO_2-CeO_2 Vegard law. Although the charge distribution has not been measured for these NPs, one can expect that the oxygen stoichiometry or O/M (with M = U + Ce) ratio is equal to 2.00 or very close to this value. The principle of electroneutrality implies that either Ce and U are both tetravalent or Ce^{III} and U^V coexist in equimolar proportions, as has been demonstrated in other doped UO_2 compounds.[11−13] It is very interesting to notice that, despite the formation of NPs having a very high surface area and the use of water in the synthesis method, the conditions are

obviously reductive enough to obtain close to stoichiometric materials. However, as presented in the next section, these particles stay very sensitive to the oxidation, and their oxidation actually takes place in the following days despite the storage of the sample in nitrogen gloveboxes.

Evolution of the NP Lattice Parameter. The $U_{1-x}Ce_xO_{2+y}$ NPs were stored in a desiccator under vacuum after flushing with argon 3 months before the HERFD−XANES measurement. During this period, XRD measurements were regularly performed to assess the evolution of their lattice parameters.

As a general trend, we can see in Figure 2 that the lattice parameter decreases with time for each composition. This evolution of the unit cell is characteristic of an oxidation process,[34] which is besides in perfect agreement with the very high specific area of the studied NPs. Considering the oxidation mechanism in UO_2,[35,36] one can assume here that U^{IV} has been oxidized into higher valence states in agreement with the O/M ratio greater than 2.00. The charge distributions of these 3 month stored NPs have been assessed using HERFD−XANES.

Charge Distribution of the Room-Temperature-Oxidized NPs. *Ce Oxidation State.* The Ce L_{III} HERFD−XANES spectra of all the investigated $U_{1-x}Ce_xO_{2+y}$ NPs, as well as Ce^{III} and Ce^{IV} references, are given in Figure 3 and compared with CeO_2 and Ce^{III} references.

Three characteristic features (A−C) are observed on the HERFD−XANES spectrum of bulk CeO_2. The pre edge peak (noted A) originates from the 2p transition to a mixed 5d−4f band/orbital/state. A doublet structure, due to the crystal field splitting of 5d states,[37] is observed for screened B (B1 + B2) and unscreened C (C1 + C2) excited states.[38,39] These arise from $2p_{3/2} \rightarrow 5d_{5/2}$ transitions.

In contrast, the HERFD−XANES spectrum of the bulk Ce^{III} reference shows only one single feature.

Regarding the HERFD−XANES spectra of the $U_{1-x}Ce_xO_{2+y}$ NPs, one can observe that the spectra are quite similar in the 5735−5750 eV region, corresponding to the C (C1 + C2) feature of the CeO_2 reference. One can then argue that this C doublet is not affected by the Ce oxidation state but mostly by the local structure (as the crystallographic structure remains the same for all compounds). However, strong differences can be observed in the 5720−5735 eV range, corresponding to the A and B features of the CeO_2 reference. In the case of $U_{0.90}Ce_{0.10}O_{2\pm x}$, the Ce L $_{III}$ threshold is strongly shifted toward lower energy, and one maximum is observed at the same energy as the Ce^{III} reference. For both $U_{0.50}Ce_{0.50}O_{2+y}$ and $U_{0.40}Ce_{0.60}O_{2+y}$ samples, the spectra look quite similar and can be compared to the shape of the CeO_2 reference, although the B_1 and B_2 positions are shifted toward lower energy. For $U_{0.17}Ce_{0.83}O_{2+y}$ and $U_{0.10}Ce_{0.90}O_{2+y}$, the spectra exhibit the same shape as the CeO_2 reference.

The Ce^{III} and Ce^{IV} molar fractions deduced from Ce L_{III} HERFD−XANES are provided in Table 2.

In addition, some papers[40] recommend using the Ce L_{III} pre edge to assess the molar fractions of Ce^{III} and Ce^{IV}. However, in our present work, the pre edges of all of our NPs have similar shape, amplitude, and position, while the features above the edge are clearly different. This shows that a proper determination of the Ce valence can only be achieved by fitting the edge region.

U Oxidation State. The oxidation state and electronic structure of U were assessed using U M_{IV} edge HERFD−
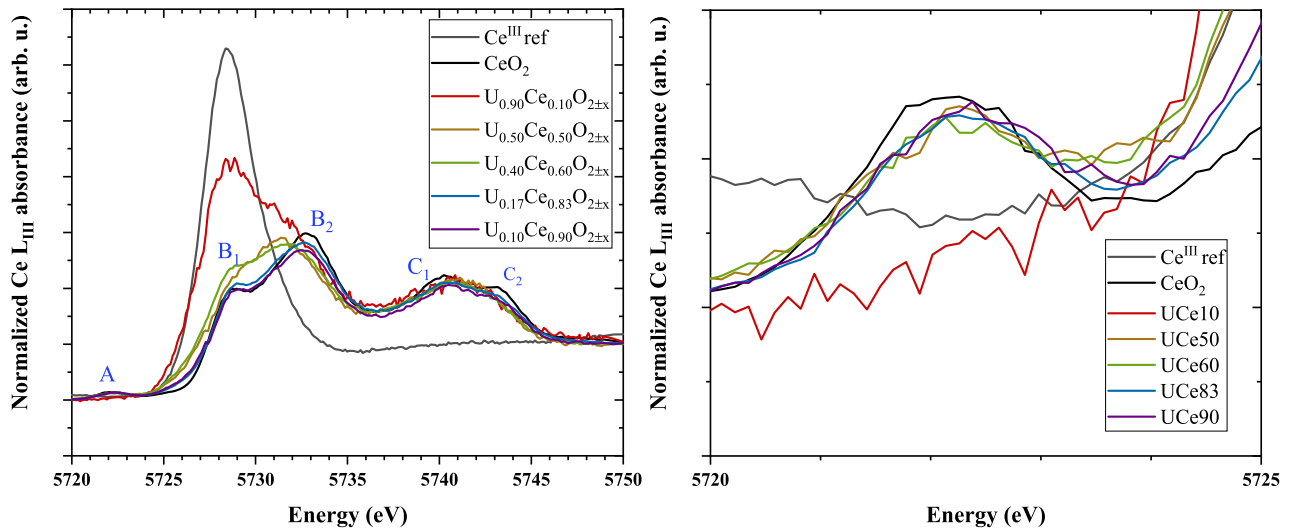
Figure 3. (Left) Ce L_{III} HERFD−XANES spectra of $U_{1−x}Ce_xO_{2+y}$ NPs compared to the CeO_2 reference. (Right) Pre edge region of the Ce L_{III} HERFD−XANES spectra.

Table 2. U and Ce Valences, Molar Fractions, and O/M Ratios Derived from the Fitting of the U M_{IV} and Ce L_{III} HERFD−XANES Spectra[a]

	U^{IV} (%)	U^V (%)	U^{VI} (%)	valence of U	Ce^{III} (%)	Ce^{IV} (%)	valence of Ce	O/M	U_{surf}* (%)
$U_{0.90}Ce_{0.10}O_{2+y}$	38 (5)	57 (5)	5 (5)	4.67	60 (5)	40 (5)	3.6	2.28 (1)	12
$U_{0.50}Ce_{0.50}O_{2+y}$	9 (5)	50 (5)	41 (5)	5.33	14 (5)	86 (5)	3.86	2.25 (1)	22
$U_{0.40}Ce_{0.60}O_{2+y}$	5 (5)	39 (5)	56 (5)	5.51	13 (5)	87 (5)	3.87	2.26 (1)	22
$U_{0.17}Ce_{0.83}O_{2+y}$	3 (5)	31 (5)	66 (5)	5.64	0	100 (5)	4	2.13 (1)	22
$U_{0.10}Ce_{0.90}O_{2+y}$	3 (5)	31 (5)	66 (5)	5.62	0	100 (5)	4	2.08 (1)	29

[a]R factors in the range of 0.2−0.6% have been achieved for the fits. *U_{surf} corresponds to the fraction of U atoms at the surface of the NPs. This fraction was derived taking into account the lattice parameter and the NP size. Uncertainties are given in brackets.

XANES. The corresponding spectra of each NP sample compared to $U^{IV}O_{2.00}$ and $(U^V_{0.67}U^{IV}_{0.33})_3O_8$ references[28] are provided in Figure 4.

As previously reported,[11,28,35,36,41−46] the various oxidation states of U are perfectly identifiable at M_{IV} edges. The HERFD−XANES spectrum of $U^{IV}O_2$ shows a sharp peak at 3725.2 (2) eV, resulting from the transition from the $3d_{5/2}$ core
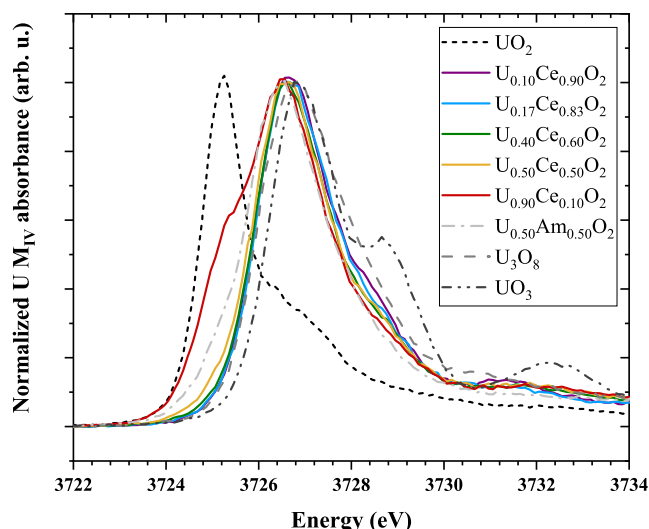

Figure 4. U M_4 HERFD−XANES spectra of $U_{1−x}Ce_xO_{2+y}$ NPs compared to UO_2, U_3O_8, UO_3, and $U_{0.50}Am_{0.50}O_2$ references.

level to the unoccupied $5f_{5/2}$ levels. The $(U^{IV}_{0.5}U^V_{0.5})_4O_9$ HERFD−XANES spectrum presents this U^{IV} characteristic feature as well as a peak at 3726.2 (2) eV corresponding to U^V. In the case of $(U^V_{0.67}U^{IV}_{0.33})_3O_8$, the HERFD−XANES spectrum exhibits a white line at 3726.9 (2) eV attributed to U^{VI}. At the lower energy side, a shoulder is observed, whose energy matches the same position as the characteristic feature of U^V in $(U^{IV}_{0.5}U^V_{0.5})_4O_9$.[28]

Except the $U_{0.90}Ce_{0.10}O_{2+y}$ U M_{IV} HERFD−XANES spectrum, all the other spectra are ranging between the U_4O_9 and U_3O_8 reference spectra. Their white line shapes are close to U_3O_8, although various intensities of the U^V and U^{VI} features are observed, suggesting varying fractions of this species. Also, one should note that the presence of U^{IV} is also clearly evidenced by its 3725.2 (2) eV feature. For $U_{0.90}Ce_{0.10}O_{2+y}$ NP, one can clearly observe a shoulder at the left side which is at the same position as the peak characteristic of U^{IV} in $U^{IV}O_2$, which confirms the presence of U^{IV}.

Charge Distribution. From the assessed molar fractions of Ce and U provided in Table 2, it is clear that the U and Ce valences are proportional. These oxidation states increase with the Ce content. For the higher content of Ce, the main valence states are U^V, U^{VI}, and Ce^{IV}. For all NPs, hyperstoichiometric materials are achieved. This is in good agreement with the strong decrease of the lattice parameter compared to the values measured on the as synthesized compounds and with the values of ionic radius.[47] We can then assume that after the synthesis, the NPs were nearly stoichiometric (as the lattice parameters are matching Vegard's law) and then oxidize during the next 3 months with the oxidation of U^{IV} into U^V and U^{VI}.
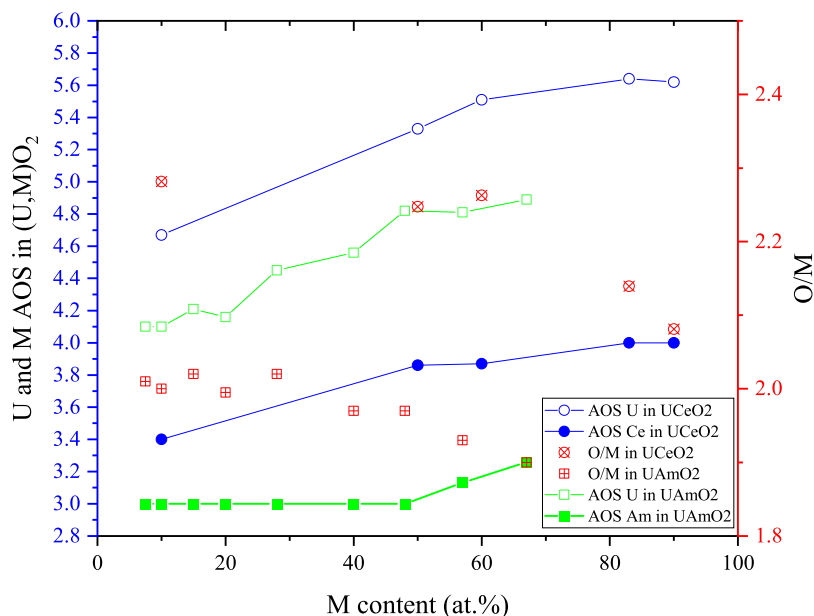
Figure 5. (Left axis) U and M AOSs and (right axis) O/M as a function of the M content in $U_{1-x}Ce_xO_{2+y}$ and $(U,Am)O_{2+y}$.

Presence of U^{VI} within the Fluorite Structure. The presence of U^{VI} has already been reported in $U_{1-x}Ce_xO_{2+y}$ thin films, but the nature of the U^{VI} phase is not discussed in this paper.[15] In Ln^{III} [48−50] and Am^{51} doped UO_2 compounds, U^{VI} was also evidenced and attributed to the presence of the $(U,M)_3O_8$ phase. For $U_{1-x}Bi_xO_{2+y}$ materials, no evidence of such $(U,M)_3O_8$ phase was found and hence U^{VI} was assumed to crystallize in the fluorite structure.[43,52] In the present work, only fluorite solid solutions are derived from XRD and no $(U,Ce)_3O_8$ is detected. Considering that we work in the presence of NPs and with bulk + surface sensitive techniques, we could assume that the molar fraction of U^{VI} in our NPs solely originates from the presence of surface species. However, except $U_{0.90}Ce_{0.10}O_{2+y}$, Table 2 shows that the number of U atoms at the surface is always lower than the U^{VI} molar fraction, which means that U^{VI} coexists with U^{IV} and U^V within the fluorite structured bulk.

Coexistence of U^{IV}, U^V, and U^{VI} within the Fluorite Structure. The coexistence of several U oxidation states in the doped UO_2 fluorite structure has already been evidenced. Indeed, it was shown that the incorporation of a nontetravalent cation in the UO_2 structure is accommodated through the formation of U^V in $U_{1-x}Am_xO_2$, $U_{1-x}La_xO_2$, $U_{1-x}Bi_xO_2$, and $U_{1-x}Gd_xO_2$ in the range $0 < x_M < 0.50$.[11,12,43,52] Doping with a trivalent cation hence results in the oxidation of U^{IV} into U^V. Remarkably, equimolar fractions of M^{III} and U^V were often measured, leading to oxygen stoichiometry very close or equal to 2.00. However, for $0.40 \leq x_{Am} \leq 0.70$, this charge compensation mechanism is no longer sufficient as the molar fraction of U^V becomes higher than that of Am^{III} and, for even higher Am content, Am^{III} starts oxidizing into Am^{IV}. These variations of the average oxidation state (AOS) of U and Am in $U_{1-x}Am_xO_2$ are given in green in Figure 5 as a function of the M content. On this plot, the AOSs of Ce and U determined in this work are also presented in blue. Overall, the tendency between $U_{1-x}Am_xO_2$ and $U_{1-x}Ce_xO_2$ NPs is similar, meaning that both U and M AOS are proportional to the M content. Even if the two systems show significant differences in terms of valence ratio, probably due to the difference of Am^{III} and Ce^{III}

stability in oxides, it is interesting to see the similarity between the two systems. Indeed, at high uranium content ($0.50 \leq x_{Am}$), Am^{III} is fully stabilized in the $U_{1-x}Am_xO_{2\pm x}$ system, even after air oxidation at high temperature.[53] Similarly, here, Ce^{III} is partially stabilized in the $U_{1-x}Ce_xO_{2\pm x}$ system, especially for low cerium content, despite the room temperature oxidation of the NPs over time.

CONCLUSIONS

In this paper, we combined XRD and HERFD−XANES to study both cation valences and oxygen stoichiometries of $U_{1-x}Ce_xO_{2+y}$. We show that the fluorite structure is maintained over the full compositional domain and independently of the U valence. Indeed, the crystallographic structure is not affected by the coexistence of U^{IV}, U^V, and U^{VI}.

AUTHOR INFORMATION

Corresponding Authors

Damien Prieur − *Institute of Resource Ecology, Helmholtz Zentrum Dresden Rossendorf (HZDR), 01314 Dresden, Germany; The Rossendorf Beamline at ESRF—The European Synchrotron, 38043 Grenoble Cedex 9, France;* orcid.org/0000 0001 5087 0133; Email: d.prieur@ hzdr.de

Jean François Vigier − *Joint Research Centre, European Commission, 76125 Karlsruhe, Germany;* orcid.org/ 0000 0002 3640 1098; Email: jean françois.vigier@ ec.europa.eu

Authors

Karin Popa − *Joint Research Centre, European Commission, 76125 Karlsruhe, Germany;* orcid.org/0000 0003 2759 6492

Olaf Walter − *Joint Research Centre, European Commission, 76125 Karlsruhe, Germany;* orcid.org/0000 0002 2679 1715

Oliver Dieste − *Joint Research Centre, European Commission, 76125 Karlsruhe, Germany*

Zsolt Varga − *Joint Research Centre, European Commission, 76125 Karlsruhe, Germany;* orcid.org/0000 0003 1910 7505

Aaron Beck − *Institute for Nuclear Waste Disposal, Karlsruhe Institute of Technology, 76021 Karlsruhe, Germany*

Tonya Vitova − *Institute for Nuclear Waste Disposal, Karlsruhe Institute of Technology, 76021 Karlsruhe, Germany;* orcid.org/0000 0002 3117 7701

Andreas C. Scheinost − *Institute of Resource Ecology, Helmholtz Zentrum Dresden Rossendorf (HZDR), 01314 Dresden, Germany; The Rossendorf Beamline at ESRF—The European Synchrotron, 38043 Grenoble Cedex 9, France;* orcid.org/0000 0002 6608 5428

Philippe M. Martin − *CEA, DEN, DMRC, SFMA, LCC, F30207 Bagnols sur Cèze Cedex, France*

Author Contributions

K.P. and O.W. carried out the NP synthesis work. J F.V, K.P., O.W., O.D., and Z.V. performed characterizations of the samples using in house laboratory equipment. D.P. and P.M.M. performed synchrotron measurements and associated data treatment. K.P., J. F.V., A.B., and T.V. set up the spectrometer for U M_{IV} and Ce L_{III} measurements. D.P., J F.V., K.P., and P.M.M. co wrote the paper. D.P., K.P., P.M.M., O.W., and A.C.S. were involved in the planning and supervision of the work. All authors discussed the results and contributed to the final manuscript.

Notes

The authors declare no competing financial interest.

REFERENCES

(1) Piro, M. H. A.; Dumas, J. C.; Lewis, B. J.; Thompson, W. T.; Iglesias, F. C. 2.07 Fission Product Chemistry in Oxide Fuels. In *Comprehensive Nuclear Materials*, 2nd ed.; Konings, R. J. M., Stoller, R. E., Eds.; Elsevier: Oxford, 2020; pp 173−199.

(2) Plakhova, T. V.; Romanchuk, A. Y.; Yakunin, S. N.; Dumas, T.; Demir, S.; Wang, S.; Minasian, S. G.; Shuh, D. K.; Tyliszczak, T.; Shiryaev, A. A.; Egorov, A. V.; Ivanov, V. K.; Kalmykov, S. N. Solubility of Nanocrystalline Cerium Dioxide: Experimental Data and Thermodynamic Modeling. *J. Phys. Chem. C* **2016**, *120*, 22615−22626.

(3) Batuk, O. N.; Szabó, D. V.; Denecke, M. A.; Vitova, T.; Kalmykov, S. N. Synthesis and Characterization of Thorium, Uranium and Cerium Oxide Nanoparticles. *Radiochim. Acta* **2013**, *101*, 233−240.

(4) Maji, D.; Ananthasivan, K.; Venkata Krishnan, R.; Balakrishnan, S.; Amirthapandian, S.; Joseph, K.; Dasgupta, A. Nanocrystalline (U0.5Ce0.5)O2±x Solid Solutions through Citrate Gel Combustion. *J. Nucl. Mater.* **2018**, *502*, 370−379.

(5) Maji, D.; Ananthasivan, K.; Venkatakrishnan, R.; Desigan, N.; Pandey, N. K. Synthesis, Characterization and Sintering of Nano crystalline (U1 YCey)O2±x. *J. Nucl. Mater.* **2021**, *547*, 152824.

(6) Nagarajan, K.; Saha, R.; Yadav, R. B.; Rajagopalan, S.; Kutty, K. V. G.; Saibaba, M.; Rao, P. R. V.; Mathews, C. K. Oxygen Potential Studies on Hypostoichiometric Uranium Cerium Mixed Oxide. *J. Nucl. Mater.* **1985**, *130*, 242−249.

(7) Venkata Krishnan, R.; Nagarajan, K. Heat Capacity Measure ments on Uranium−Cerium Mixed Oxides by Differential Scanning Calorimetry. *Thermochim. Acta* **2006**, *440*, 141−145.

(8) Venkata Krishnan, R.; Panneerselvam, G.; Singh, B. M.; Kothandaraman, B.; Jogeswararao, G.; Antony, M. P.; Nagarajan, K. Synthesis, Characterization and Thermal Expansion Measurements on Uranium−Cerium Mixed Oxides. *J. Nucl. Mater.* **2011**, *414*, 393−398.

(9) Gasperi, G.; Amidani, L.; Benedetti, F.; Boscherini, F.; Glatzel, P.; Valeri, S.; Luches, P. Electronic Properties of Epitaxial Cerium Oxide Films during Controlled Reduction and Oxidation Studied by Resonant Inelastic X Ray Scattering. *Phys. Chem. Chem. Phys.* **2016**, *18*, 20511−20517.

(10) Hofmann, K. A.; Höschele, K. Das Magnesiumchlorid Als Mineralisator. II.: Das Urancerblau Und Das Wesen Der Konstitu tiven Färbung. Das Magnesiarot Und Das Magnesiagrün. *Ber. Dtsch. Chem. Ges.* **1915**, *48*, 20−28.

(11) Prieur, D.; Martel, L.; Vigier, J. F.; Scheinost, A. C.; Kvashnina, K. O.; Somers, J.; Martin, P. M. Aliovalent Cation Substitution in UO2: Electronic and Local Structures of U1−YLayO2±x Solid Solutions. *Inorg. Chem.* **2018**, *57*, 1535−1544.

(12) Prieur, D.; Martin, P.; Lebreton, F.; Delahaye, T.; Banerjee, D.; Scheinost, A. C.; Jankowiak, A. Accommodation of Multivalent Cations in Fluorite Type Solid Solutions: Case of Am Bearing UO2. *J. Nucl. Mater.* **2013**, *434*, 7−16.

(13) Prieur, D.; Martin, P. M.; Jankowiak, A.; Gavilan, E.; Scheinost, A. C.; Herlet, N.; Dehaudt, P.; Blanchart, P. Local Structure and Charge Distribution in Mixed Uranium Americium Oxides: Effects of Oxygen Potential and Am Content. *Inorg. Chem.* **2011**, *50*, 12437−12445.

(14) Markin, T. L.; Street, R. S.; Crouch, E. C. The Uranium Cerium Oxygen Ternary Phase Diagram. *J. Inorg. Nucl. Chem.* **1970**, *32*, 59−75.

(15) Eloirdi, R.; Cakir, P.; Huber, F.; Seibert, A.; Konings, R.; Gouder, T. X Ray Photoelectron Spectroscopy Study of the Reduction and Oxidation of Uranium and Cerium Single Oxide Compared to (U Ce) Mixed Oxide Films. *Appl. Surf. Sci.* **2018**, *457*, 566−571.

(16) Prieur, D.; Bonani, W.; Popa, K.; Walter, O.; Kriegsman, K. W.; Engelhard, M. H.; Guo, X.; Eloirdi, R.; Gouder, T.; Beck, A.; Vitova, T.; Scheinost, A. C.; Kvashnina, K.; Martin, P. Size Dependence of Lattice Parameter and Electronic Structure in CeO2 Nanoparticles. *Inorg. Chem.* **2020**, *59*, 5760.

(17) Plakhova, T. V.; Romanchuk, A. Y.; Likhosherstova, D. V.; Baranchikov, A. E.; Dorovatovskii, P. V.; Svetogorov, R. D.; Shatalova, T. B.; Egorova, T. B.; Trigub, A. L.; Kvashnina, K. O.; Ivanov, V. K.; Kalmykov, S. N. Size Effects in Nanocrystalline Thoria. *J. Phys. Chem. C* **2019**, *123*, 23167−23176.

(18) Amidani, L.; Plakhova, T. V.; Romanchuk, A. Y.; Gerber, E.; Weiss, S.; Efimenko, A.; Sahle, C. J.; Butorin, S. M.; Kalmykov, S. N.; Kvashnina, K. O. Understanding the Size Effects on the Electronic Structure of ThO2 Nanoparticles. *Phys. Chem. Chem. Phys.* **2019**, *21*, 10635−10643.

(19) Sutter, E.; Sutter, P. Size Dependent Room Temperature Oxidation of In Nanoparticles. *J. Phys. Chem. C* **2012**, *116*, 20574−20578.

(20) Walter, O.; Popa, K.; Blanco, O. D. Hydrothermal Decomposition of Actinide(IV) Oxalates: A New Aqueous Route towards Reactive Actinide Oxide Nanocrystals. *Open Chem.* **2016**, *14*, 170−174.

(21) Popa, K.; Walter, O.; Blanco, O. D.; Guiot, A.; Bouëxière, D.; Colle, J. Y.; Martel, L.; Naji, M.; Manara, D. A Low Temperature Synthesis Method for AnO2 Nanocrystals (An = Th, U, Np, and Pu) and Associate Solid Solutions. *CrystEngComm* **2018**, *20*, 4614−4622.

(22) Vălu, S. O.; Bona, E. D.; Popa, K.; Griveau, J. C.; Colineau, E.; Konings, R. J. M. The Effect of Lattice Disorder on the Low Temperature Heat Capacity of (U 1−y Th y)O 2 and 238 Pu Doped UO 2. *Sci. Rep.* **2019**, *9*, 15082.

(23) Petříček, V.; Dušek, M.; Palatinus, L. Crystallographic Computing System JANA2006: General Features. *Z. für Kristallogr. Cryst. Mater.* **2014**, *229*, 345−352.

(24) Glatzel, P.; Bergmann, U. High Resolution 1s Core Hole X Ray Spectroscopy in 3d Transition Metal Complexes—Electronic and Structural Information. *Coord. Chem. Rev.* **2005**, *249*, 65−95.

(25) Zimina, A.; Dardenne, K.; Denecke, M. A.; Grunwaldt, J. D.; Huttel, E.; Lichtenberg, H.; Mangold, S.; Pruessmann, T.; Rothe, J.; Steininger, R.; Vitova, T. The CAT ACT Beamline at ANKA: A New High Energy X Ray Spectroscopy Facility for CATalysis and ACTinide Research. *J. Phys.: Conf. Ser.* **2016**, *712*, 012019.

(26) Zimina, A.; Dardenne, K.; Denecke, M. A.; Doronkin, D. E.; Huttel, E.; Lichtenberg, H.; Mangold, S.; Pruessmann, T.; Rothe, J.; Spangenberg, T.; Steininger, R.; Vitova, T.; Geckeis, H.; Grunwaldt, J. D. CAT ACT—A New Highly Versatile x Ray Spectroscopy Beamline for Catalysis and Radionuclide Science at the KIT Synchrotron Light Facility ANKA. *Rev. Sci. Instrum.* **2017**, *88*, 113113.

(27) Glatzel, P.; Weng, T. C.; Kvashnina, K.; Swarbrick, J.; Sikora, M.; Gallo, E.; Smolentsev, N.; Mori, R. A. Reflections on Hard X Ray Photon in/Photon out Spectroscopy for Electronic Structure Studies. *J. Electron Spectrosc. Relat. Phenom.* **2013**, *188*, 17−25.

(28) Kvashnina, K. O.; Butorin, S. M.; Martin, P.; Glatzel, P. Chemical State of Complex Uranium Oxides. *Phys. Rev. Lett.* **2013**, *111*, 253002.

(29) Epifano, E.; Naji, M.; Manara, D.; Scheinost, A. C.; Hennig, C.; Lechelle, J.; Konings, R. J. M.; Guéneau, C.; Prieur, D.; Vitova, T.; Dardenne, K.; Rothe, J.; Martin, P. M. Extreme Multi Valence States in Mixed Actinide Oxides. *Commun. Chem.* **2019**, *2*, 59.

(30) Martin, P.; Ripert, M.; Petit, T.; Reich, T.; Hennig, C.; D'Acapito, F.; Hazemann, J. L.; Proux, O. A XAS Study of the Local Environments of Cations in (U, Ce)O2. *J. Nucl. Mater.* **2003**, *312*, 103−110.

(31) Yamada, K.; Yamanaka, S.; Nakagawa, T.; Uno, M.; Katsura, M. Study of the Thermodynamic Properties of (U, Ce)O2. *J. Nucl. Mater.* **1997**, *247*, 289−292.

(32) Kim, D. J.; Kim, Y. S.; Kim, S. H.; Kim, J. H.; Yang, J. H.; Lee, Y. W.; Kim, H. S. The Linear Thermal Expansion and the Thermal Diffusivity Measurements for Near Stoichiometric (U, Ce)O2 Solid Solutions. *Thermochim. Acta* **2006**, *441*, 127−131.

(33) Bera, S.; Mittal, V. K.; Venkata Krishnan, R.; Saravanan, T.; Velmurugan, S.; Nagarajan, K.; Narasimhan, S. V. XPS Analysis of UxCe1−xO2±δ and Determination of Oxygen to Metal Ratio. *J. Nucl. Mater.* **2009**, *393*, 120−125.

(34) Prieur, D.; Carvajal Nunez, U.; Somers, J. O/M Ratio Determination and Oxidation Behaviour of Th0.8Am0.20O2 x. *J. Nucl. Mater.* **2013**, *435*, 49−51.

(35) Desfougeres, L.; Welcomme, É.; Ollivier, M.; Martin, P. M.; Hennuyer, J.; Hunault, M. O. J. Y.; Podor, R.; Clavier, N.; Favergeon, L. Oxidation as an Early Stage in the Multistep Thermal Decomposition of Uranium(IV) Oxalate into U3O8. *Inorg. Chem.* **2020**, *59*, 8589.

(36) Manaud, J.; Maynadié, J.; Mesbah, A.; Hunault, M. O. J. Y.; Martin, P. M.; Zunino, M.; Meyer, D.; Dacheux, N.; Clavier, N. Hydrothermal Conversion of Uranium(IV) Oxalate into Oxides: A Comprehensive Study. *Inorg. Chem.* **2020**, *59*, 3260−3273.

(37) Paun, C.; Safonova, O. V.; Szlachetko, J.; Abdala, P. M.; Nachtegaal, M.; Sa, J.; Kleymenov, E.; Cervellino, A.; Krumeich, F.;

van Bokhoven, J. A. Polyhedral CeO2 Nanoparticles: Size Dependent Geometrical and Electronic Structure. *J. Phys. Chem. C* **2012**, *116*, 7312−7317.

(38) Bianconi, A.; Marcelli, A.; Dexpert, H.; Karnatak, R.; Kotani, A.; Jo, T.; Petiau, J. Specific Intermediate Valence State of Insulating 4f Compounds Detected by ${L}$ ${3}$ x Ray Absorption. *Phys. Rev. B: Condens. Matter Mater. Phys.* **1987**, *35*, 806−812.

(39) Soldatov, A. V.; Ivanchenko, T. S.; Kotani, A.; Bianconi, A. L3 Edge X Ray Absorption Spectrum of CeO2: Crystal Structure Effects. *Phys. B* **1995**, *208−209*, 53−55.

(40) Cafun, J. D.; Kvashnina, K. O.; Casals, E.; Puntes, V. F.; Glatzel, P. Absence of Ce3+ Sites in Chemically Active Colloidal Ceria Nanoparticles. *ACS Nano* **2013**, *7*, 10726−10732.

(41) Vitova, T.; Denecke, M. A.; Goettlicher, J.; Jorissen, K.; Kas, J. J.; Kvashnina, K.; Pruessmann, T.; Rehr, J. J.; Rothe, J. Actinide and Lanthanide Speciation with High Energy Resolution X Ray Techni ques. *15th International Conference on X ray Absorption Fine Structure (XAFS15)*; Wu, Z. Y., Eds.; IOP Publishing Ltd.: Bristol, 2013; Vol. 430, p UNSP012117.

(42) Butorin, S. M.; Kvashnina, K. O.; Smith, A. L.; Popa, K.; Martin, P. M. Crystal Field and Covalency Effects in Uranates: An X Ray Spectroscopic Study. *Chem.—Eur. J.* **2016**, *22*, 9693−9698.

(43) Popa, K.; Prieur, D.; Manara, D.; Naji, M.; Vigier, J. F.; Martin, P. M.; Dieste Blanco, O.; Scheinost, A. C.; Prüβmann, T.; Vitova, T.; Raison, P. E.; Somers, J.; Konings, R. J. M. Further Insights into the Chemistry of the Bi U O System. *Dalton Trans.* **2016**, *45*, 7847−7855.

(44) Butorin, S. M.; Kvashnina, K. O.; Prieur, D.; Rivenet, M.; Martin, P. M. Characteristics of Chemical Bonding of Pentavalent Uranium in La Doped UO2. *Chem. Commun.* **2017**, *53*, 115−118.

(45) Pidchenko, I.; Kvashnina, K. O.; Yokosawa, T.; Finck, N.; Bahl, S.; Schild, D.; Polly, R.; Bohnert, E.; Rossberg, A.; Göttlicher, J.; Dardenne, K.; Rothe, J.; Schäfer, T.; Geckeis, H.; Vitova, T. Uranium Redox Transformations after U(VI) Coprecipitation with Magnetite Nanoparticles. *Environ. Sci. Technol.* **2017**, *51*, 2217−2225.

(46) Kauric, G.; Walter, O.; Beck, A.; Schacherl, B.; Dieste Blanco, O.; Vigier, J. F.; Zuleger, E.; Vitova, T.; Popa, K. Synthesis and Characterization of Nanocrystalline U1 XPuxO2(+y) Mixed Oxides. *Mater. Today Adv.* **2020**, *8*, 100105.

(47) Shannon, R. D. Revised Effective Ionic Radii and Systematic Studies of Interatomic Distances in Halides and Chalcogenides. *Acta Crystallogr., Sect. A: Cryst. Phys., Diffr., Theor. Gen. Crystallogr.* **1976**, *32*, 751−767.

(48) Razdan, M.; Shoesmith, D. W. Influence of Trivalent Dopants on the Structural and Electrochemical Properties of Uranium Dioxide (UO2). *J. Electrochem. Soc.* **2013**, *161*, H105.

(49) Kim, J. G.; Ha, Y. K.; Park, S. D.; Jee, K. Y.; Kim, W. H. Effect of a Trivalent Dopant, Gd3+, on the Oxidation of Uranium Dioxide. *J. Nucl. Mater.* **2001**, *297*, 327−331.

(50) Herrero, B.; Bès, R.; Audubert, F.; Clavier, N.; Hunault, M. O. J. Y.; Baldinozzi, G. Charge Compensation Mechanisms in Nd Doped UO2 Samples for Stoichiometric and Hypo Stoichiometric Con ditions: Lack of Miscibility Gap. *J. Nucl. Mater.* **2020**, *539*, 152276.

(51) Caisso, M.; Roussel, P.; Den Auwer, C.; Picart, S.; Hennig, C.; Scheinost, A. C.; Delahaye, T.; Ayral, A. Evidence of Trivalent Am Substitution into U3O8. *Inorg. Chem.* **2016**, *55*, 10438−10444.

(52) Bès, R.; Rivenet, M.; Solari, P. L.; Kvashnina, K. O.; Scheinost, A. C.; Martin, P. M. Use of HERFD XANES at the U L 3 and M 4 Edges To Determine the Uranium Valence State on [Ni(H2O)(4)] (3)[U(OH,H2O)(UO2)(8)O 12(OH)(3)]. *Inorg. Chem.* **2016**, *55*, 4260−4270.

(53) Epifano, E.; Vauchy, R.; Lebreton, F.; Lauwerier, R.; Joly, A.; Scheinost, A.; Guéneau, C.; Valot, C.; Martin, P. M. On the O Rich Domain of the U Am O Phase Diagram. *J. Nucl. Mater.* **2020**, *531*, 151986.

Repository KITopen

Dies ist ein Postprint/begutachtetes Manuskript.

Empfohlene Zitierung:

Zitierung der Originalveröffentlichung: